Microporous Membranes of Polyoxymethylene from a Melt-Extrusion Process: (I) Effects of Resin Variables and Extrusion Conditions

MATTHEW B. JOHNSON,* GARTH L. WILKES

Virginia Tech, Polymer Materials and Interfaces Laboratory and Department of Chemical Engineering, Blacksburg, Virginia 24061

Received 19 September 2000; accepted 9 October 2000

ABSTRACT: A two-part study utilizing polyoxymethylene (POM) was undertaken to investigate a three stage process (melt extrusion/annealing/uniaxial stretching) (MEAUS) employed to produce microporous films. In this first part, three POM resins (D, E, and F) were melt extruded into tubular films (blowup ratio; BUR = 1), where resin D has a higher weight average molecular weight (M_w) than resin E, but both possess similar and relatively narrow molecular-weight distributions (MWD). In contrast, resin F is characterized by a distinctly broader MWD while its M_w is slightly higher than resin D. Specific attention was focused upon the morphological and crystal orientation results as a function MWD and M_w. A stacked lamellar morphology was obtained in each case from the melt extrusion; however, the type of stacked lamellar morphology, planar or twisted, and the orientation state was found to depend upon both the resin characteristics and the melt-extrusion conditions. Atomic force microscopy and wide-angle X-ray scattering were the main techniques utilized to study the melt-extruded films while dynamic melt rheometry in conjunction with the Carreau-Yasuda model aided in differentiating the melt-flow behavior of the three resins. Small-angle light scattering (SALS) was also employed to characterize the morphological state. © 2001 John Wiley & Sons, Inc. J Appl Polym Sci 81: 2944–2963, 2001

Key words: processing; melt extrusion; polyoxymethylene; POM; stacked lamellae

INTRODUCTION

In a similar investigation[1] by the authors, isotactic poly(4-methyl-1-pentene) (PMP) was studied in a sequential manner from resin to final film with respect to the three-stage (melt-extrusion/annealing/uniaxial-stretching) (MEAUS) method utilized to produce microporous membranes. From this study, the authors verified a number of prerequisites for microporous membrane formation via the method in question. The first prerequisite is the ability of the oriented polymer to crystallize at a sufficient rate so that main-chain melt relaxation does not occur during extrusion. Fast crystallization kinetics then enable a tubular film (blowup ratio; BUR = 1) to be produced with a planar stacked lamellar morphology (little or no lamellar twisting) and "high" crystalline orientation. Also, it is undesirable to have a high concentration of long fibril nuclei similar to the structures reported by Yu and coworkers[2] for linear high-density polyethylene (HDPE) tubular films, which were found to "pin" the lamellae together during uniaxial-stretching (third stage). A rapid quenching process and control of the film thickness to approximately 1 mil (25 μm), which

* *Present address:* 3M Center, St. Paul, MN.
Correspondence to: G. Wilkes (gwilkes@vt.edu).
Contract grant sponsor: Celgard Corporation LLC.

Journal of Applied Polymer Science, Vol. 81, 2944–2963 (2001)

then minimizes any skin-core effects, also facilitate a uniform parallel planar texture and "high" crystalline orientation throughout the film cross-section. The last prerequisite proposed by the authors is the ability of the polymer chains to translate through the crystal phase at a temperature below the T_m. This thermally activated transition is conventionally referred to as the α_c relaxation, and greater detail regarding its origin is presented elsewhere.[3,4] The PMP α_c relaxation was suggested to be required if a microporous membrane was to be obtained by the MEAUS process. Further evidence for this supposition exists, for both HDPE[4] and isotactic polypropylene (iPP)[4] are known to possess an α_c relaxation and microporous films of each are commercially available via the MEAUS process.[5] Because this hypothesis has been verified for three polyolefin materials (HDPE, iPP, PMP), it is of interest to test the α_c supposition utilizing a nonpolyolefin highly crystalline polymer.

A semicrystalline polymer known to possess an α_c relaxation, that is, not a polyolefin, is polyoxymethylene (POM). Although this polymer has been shown to be capable of forming a microporous structure,[6,7] it has not been investigated specifically with this in mind. Instead, it was studied for its ability to display "hard-elastic" character when processed using the proper melt conditions. Additionally, there has not been a sequential study of POM from resin to final film with respect to the MEAUS method. Besides hoping to verify the proposed criteria for a nonpolyolefin, if produced into a final film possessing highly interconnected micropores, a POM membrane could serve in applications requiring a somewhat more hydrophilic film than the polyolefin membranes currently available. For example, HDPE and iPP membranes are utilized in microfiltration applications as well as battery separators between the cathode and the anode in an electrolyte solution.[8] The sequential investigation of POM from resin to final film utilizing the MEAUS method will be undertaken in the course of two articles. This first article addresses the melt-extrusion stage where the results of a number of melt-extrusion conditions applied to three different POM resins will be presented. The effect the extrusion conditions and the resin characteristics have on the resulting precursor film morphology and crystal orientation will be analyzed. The main goal is to produce a precursor with a "high" crystal orientation and a stacked lamellar morphology where the lamellae are characterized as planar, and that facilitate micropore formation via lamellar splaying (separation) during the uniaxial-stretching stage that will be addressed in part II[9] of this work.

The precursor properties of interest are the crystalline orientation, the morphology, the level of crystallinity, the melting point of the crystalline phase, and the α_c relaxation. The first was followed via wide-angle X-ray scattering (WAXS) and quantitatively evaluated using Hermans' orientation function (f_H). The morphology of the extruded film has been studied with the aid of atomic force microscopy (AFM). Small-angle light scattering (SALS) also has, in some instances, been employed to observe structures on the order of the wave length of light. For example, H_v SALS (horizontal polarizer and vertical analyzer) of an undeformed optically anisotropic spherulitic morphology typically yields a symmetric four-lobed pattern termed the "cloverleaf" pattern that possesses fourfold symmetry.[10] Such unoriented optically anisotropic spherulitic superstructures are not normal for flow-induced morphologies, but have been observed in the case of linear low-density PE blown (BUR $>$ 1) and cast roll films where near fourfold symmetry of the H_v SALS patterns were found in some instances.[11] For isotactic poly(1-butene) (PB-1) tubular extruded films, studied by Hashimoto and coworkers,[12] "butterfly-type" H_v SALS patterns occurred, which stemmed from isolated sheaf-like structures. Thus, the SALS technique has been previously employed for investigating tubular or blown film, and was utilized here for the POM precursors to observe if there are anisotropic superstructures on the scale of the wavelength of light. Small-angle X-ray scattering (SAXS) was employed to estimate the long spacing of the stacked lamellae that compose the precursors while differential scanning calorimetry (DSC) was used to assist in determining the melting point and level of crystallinity.

Considerable effort has been devoted to studying the crystalline structure and orientation state of extruded semicrystalline films by a variety of techniques including those previously listed. The row nucleated lamellae model as a result of fibril nucleation proposed by Keller and Machin[13] is accepted in many studies as a common feature of melt-extruded films or more generally for crystallization under extrusion stress. The level of this stress has also been shown to influence the final film properties. A "low" stress condition results in widely spaced fibril nuclei that are aligned along

the principal flow direction, i.e., the machine direction (MD). Lamellae nucleate from the fibrillar structures often become twisted ribbon-like structures as a result of the wide spacing between fibril nuclei. It is, however, questionable whether lamellar twisting occurs for all semicrystalline polymers, and if lamellar twisting may also be a function of the molecular weight distribution (MWD). Thus, this morphology may not be present in all materials extruded under "low" stress conditions. Crystallization under "high" stress also produces highly aligned fibril nuclei; however, these structures are more concentrated, which then produces a more parallel planar (nontwisted) lamellar morphology. Regarding polyethylene (PE), the latter extrusion stress case results in a "c"-axis orientation diffraction pattern while the low stress case produces signs of "a"-axis orientation caused by the twisted or tilted lamellae.

Based upon the suggested criteria for the formation of a highly interconnected microporous structure, the latter or "high"-stress extrusion condition produces the desired outcome. The stress applied to the melt is actually a consequence of the melt-extrusion variables such as extrusion temperature, extrusion rate, quench height, and line speed (or uptake). The molecular characteristics of the resin, for example, weight-average molecular weight (M_w) and MWD, also are known to play critical roles in the precursor properties.[1,2,14–18] For both melt-extrusion conditions and resin characteristics, it is the effect either variable has on the orientation state of the molecular conformations of the melt, specifically the degree of chain extension prior to crystallization, that is a crucial factor influencing the morphology and crystalline orientation.[15] Thus, the melt-extruded film morphology and orientation provide a window into the melt-flow behavior prior to crystallization while the degree of chain extension in the melt influences the precursor properties. In this work, the authors will present a number of stacked lamellar morphologies observed in POM extruded tubular films. The formation of these morphologies will be shown to depend mainly upon the resin characteristics and, therefore, a consequence of the melt flow/relaxation behavior of the resin during crystallization initiated at the air ring. A number of these precursors will then be selected based upon their morphologies and crystalline orientations for thermal annealing followed by uniaxial stretching along MD, i.e., the second and third stages, respectively, of the MEAUS process. In these subsequent stages, a number of variable combinations will be explored for their influence on structure and orientation with the overall goal of producing a highly uniform microporosity throughout the final film. The results from the second and third stages, however, will be presented and discussed within a later report.[9]

EXPERIMENTAL

Materials

Two POM resins designated as resins D and F were mainly employed in this study; however, a third resin labeled E was also investigated albeit to a lesser extent. Two of the three commercial resins (D and E) are a result of the same anionic polymerization of formaldehyde and end-capping the chains using acetic anhydride. The acetic anhydride is employed to stabilize the chain because POM has a relatively low ceiling temperature (ca. 120°C) and the chain undergoes depolymerization (unzipping) initiated at the hydroxyl end groups without end-capping. Resins D and E resins differ in M_w and M_n, but both possess a MWD of approximately 2. The third resin, F, is polymerized via a ring-opening polymerization mechanism. This particular synthesis utilizes a small amount of the comonomer ethylene oxide to provide thermal stability to the POM chain.[19] Additionally, and of significance to this study, resin F is characterized by a distinctly broader MWD (ca. 6.82) than either resins D or E. More information addressing the three resins will be provided in the Results section.

Melt Rheological Characterization

The three resin samples were compression molded at 180°C for a total time of 10 min. The samples were allowed to melt at atmospheric conditions for 4 min and then subjected to a low molding pressure for an additional 6 min. The molded samples were subsequently quenched under ambient conditions upon removal from the press. The 25.4-mm diameter compression-molded disks were of 2 mm in thickness. The modulus of the complex viscosity ($|\eta^*|$) as a function of frequency (ω) in radians/s was obtained by a RMS Rheometrics 800 Spectrometer using a parallel-plate geometry. The rheometer test chamber was operated with a nitrogen atmosphere to minimize polymer degradation. The

rheometer was preheated to the testing temperature of 180°C and allowed to reach thermal equilibration before loading of the specimens. The samples were squeezed between the plates to a thickness of 1.5 mm; at this time the excess sample was trimmed. From sample insertion and trimming to initiating the frequency sweep, a total time of 10 min elapsed.

The $|\eta^*|$ vs. ω data were curve fitted using the modified three-parameter Carreau-Yasuda (CY) model, eq. (1), to obtain the CY parameters: η_0, the zero shear viscosity, "a" the parameter that describes severity or sharpness of the transition from Newtonian to shear thinning behavior, and τ_n the characteristic melt-relaxation time that is correlated to the frequency where shear-thinning begins. The power law number (n), when set equal to 2/11, provided accurate CY fits to the POM rheological data and thus was held constant to lower the number of fitting parameters. Further details regarding the CY model may be found elsewhere.[20–23]

$$|\eta^*(\omega)| = \frac{\eta_o}{[1 + (\omega\tau_n)^a]^{(1-n)/a}} \quad (1)$$

Another parameter that has been used[11] to aid in understanding the melt-flow behavior is the recoverable shear strain parameter (RSP or γ_∞), which is a measure of the melt elasticity. The RSP can be described mathematically as shown in eq. (2).

$$\gamma_\infty = \frac{N_1}{2\tau} \quad (2)$$

The parameter N_1 is the first normal stress difference, and τ is the shear stress, which is equal to $|\eta^*(\omega)| \cdot \omega$ in the limit of zero shear rate. If the empirical Cox-Merz[24] rule, $(\eta(\dot{\gamma}) = |\eta^*(\omega)|_{\omega=\dot{\gamma}})$, is applied, the frequency dependent viscosity can be related to the shear rate-dependent viscosity. It can also be shown that the first normal stress can be approximated by the elastic component of the complex shear modulus (G') in the limit of ω approaching zero[25]; mathematically this becomes:

$$\lim_{\omega\to 0} N_1 = 2 \cdot G' \quad (3)$$

Therefore, using the above allows eq. (2) to be rewritten at low frequencies as,

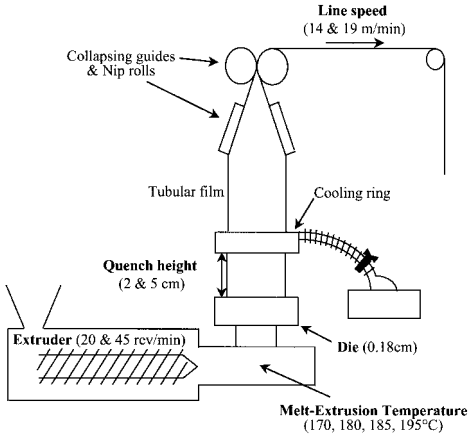

Figure 1 Schematic depicting the tubular extrusion setup utilized in this study with some processing parameters indicated.

$$RSP = \gamma_\infty \sim \frac{G'}{\omega|\eta^*(\omega)|} \quad (4)$$

It is eq. (4) that will be utilized to estimate the elasticity of the melt at low frequency (<0.05 radian/s) and provide a basis for better understanding and differentiating the melt-flow behavior of these resins.

Tubular Film Processing

All the tubular film (1 : 1 blowup ratio) samples were of 1 mil (25 μm) thickness, and all were made on a laboratory-scale blown film line. This film line was comprised of a MPM brand extruder using an annular die with a diameter of 3 inches (76 mm), a die gap of 0.070 inches (1.8 mm), a single screw with a 1.5 inch (37.5 mm) diameter (aspect ratio, L/D = 36). Films were quenched with a single-lip Western air-ring system using ambient air ca. 25°C. A schematic of the tubular film extruder is shown in Figure 1, with the important features labeled with the extrusion conditions utilized. Four main processing parameters: melt extrusion temperature, T_{melt}, extrusion speed of the screw in revolutions per minute (rpm), quench height, which is the distance from the die exit to the cooling ring, and the line speed in meters per minute (mpm) are listed with the specific conditions utilized in Tables I–III for the resins D, E, and F, respectively. In the case of resin E, three extrusion conditions were utilized, and these matched three of the conditions for resin D and one condition for resin F. The extrusion setup promotes planar extensional flow with

Table I Summary of Melt-Extrusion Conditions for Resin D

Sample	Extrusion Condition	Melt Temperature (°C)	Extrusion Speed (rpm)	Quench Height (cm)	Line Speed (mpm)
D1	1	185	40	2	14
D2	2	180	40	2	14
D3	3	195	40	2	14
D4	4	185	20	2	9
D5	5	195	20	2	9
D6	6	185	40	5	14

the deformation direction along the MD. This leads to expected uniaxial symmetry about the MD axis,[1,2] as will be verified later by WAXS and refractometry.

In all cases, the line speed was adjusted to maintain a nominal film thickness of 1 mil (25 microns). Further, the flow rate of the air through the air ring was kept constant in this study whereas, in a previous publication[2] from this laboratory that addressed HDPE, this variable was investigated utilizing a similar extrusion scheme.

Structural and Optical Techniques and Analysis Utilized

Wide-Angle X-ray Scattering (WAXS)

WAXS studies were performed on a Philips tabletop X-ray generator model PW1720 equipped with a standard vacuum sealed Warhus photographic pinhole camera. The X-ray beam was of Cu Kα radiation, $\lambda = 1.544$ Å, and was collimated to a beam diameter of 0.020 inches (0.508 mm).

As will be shown later, the planar extensional flow along the MD promoted uniaxial orientation behavior along this same axis. A commonly reported parameter for uniaxially oriented systems is a second moment average, termed the Hermans' orientation, and is expressed by eq. (5).[16]

$$f_H = \frac{(3 \cdot \overline{\cos^2\theta} - 1)}{2} \tag{5}$$

The quantity $\overline{\cos^2\theta}$ represents the average value of $\cos^2\theta$ taken over all the polymer chains within the system or phase being measured. The value for θ is the angle between the chain axis and the chosen reference axis. Therefore, if all the chains are perfectly oriented along the reference direction, then $\theta = 0°$ and $f_H = 1$. In contrast, if the chain is oriented perpendicular to that of the reference direction, then $\theta = 90°$ and $f_H = -\frac{1}{2}$. It can be shown for random orientation that $\overline{\cos^2\theta} = \frac{1}{3}$ and thus $f_H = 0$.

The most common means used to determine f_H for the crystalline orientation of a material is via WAXS. In the crystalline phase, the c-axis unit cell orientation is desirable because it generally provides the chain axis orientation. For melt-crystallized POM, the unit cell is trigonal (or hexagonal) with the unit cell dimension of "a" equal to 4.47 Å and "c" equals 17.39 Å where the "a" and "b" axes are one in the same.[26] Figure 2 depicts the coordinate system used to define a hexagonal unit cell with respect to a given set of orthogonal (x, y, z) axes. The angles α, β, and ε are measured with respect to the reference axis, z-axis, or MD, and the a, b, and c unit cell axes. In the case of a hexagonal unit cell and uniaxial symmetry, f_a equals f_b ($\alpha = \beta$), leading to,

$$2 \cdot f_a + f_c = 0 \tag{6}$$

Hence, only a single reflection that is solely dependent on the "a"-axis (h00) or "c"-axis (001) is

Table II Summary of Melt-Extrusion Conditions for Resin E

Sample	Extrusion Condition	Melt Temperature (°C)	Extrusion Speed (rpm)	Quench Height (cm)	Line Speed (mpm)
E1	1	185	40	2	14
E2	2	180	40	2	14
E4	4	185	20	2	9

Table III Summary of Melt-Extrusion Conditions for Resin F

Sample	Extrusion Condition	Melt Temperature (°C)	Extrusion Speed (rpm)	Quench Height (cm)	Line Speed (mpm)
F1	1	170	40	2	14
F2	2	180	40	2	14
F3	3	170	20	2	9
F4	4	180	20	2	9
F5	5	170	40	5	14

required to follow crystal orientation for a uniaxially oriented system. For uniaxially oriented POM materials, the set of planes typically followed are the (100) planes.[27–30] The three-index notation is employed here; however, hexagonal unit cells can also be described by four-index notation. In that case, the notation used to describe the (100) planes would be $(10\bar{1}0)$. Hermans' orientation function can be shown to become[31]

$$f_{100} = \frac{(3 \cdot \cos^2\theta_{100} \cdot \overline{\sin^2\psi_{100}} - 1)}{2} \tag{7}$$

where the azimuthal dependence of the scattered intensity for the (100) reflection is defined by the angle ψ_{100}, and θ_{100} is the Bragg angle. The quantity $\overline{\sin^2\psi_{hkl}}$ is calculated by determining the scattering intensity of the appropriate scattering reflection as a function of angle. It is represented by the following relationship

$$\overline{\sin^2\psi_{100}} = \frac{\int_0^{\pi/2} I(\psi)\sin^2\psi_{100}\cos\,\theta_{200}\,d\psi}{\int_0^{\pi/2} I(\psi)\,\cos\,\theta_{100}\,d\psi} \tag{8}$$

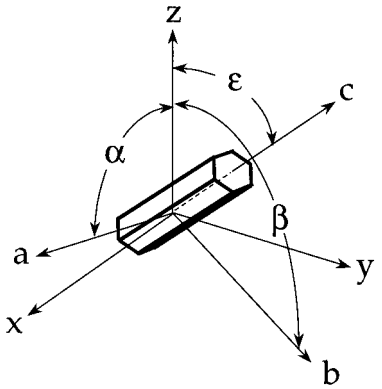

Figure 2 Coordinate system used to define the hexagonal unit cell with respect to a given set of orthogonal axes.

where $I(\psi_{100})$ is the relative intensity at the angle ψ_{100} for the (100) reflection. Equation (8) can also be evaluated graphically,[31–33] or $\overline{\sin^2\psi_{100}}$ may be approximated in uniaxial systems by measuring the half width of the (100) arc.[31–33] Thus, the crystalline orientation can be estimated by examination of the azimuthal angle dependence of the (100) reflection obtained from standard flat plate WAXS patterns.

Birefringence

Optical anisotropy or birefringence is another means of measuring the Hermans' orientation function in single-phase systems owing to the following equation

$$\Delta_T = \Delta^\circ \cdot f_c \tag{9}$$

where Δ_T is the birefringence of the material under investigation, and Δ° is the birefringence of the fully oriented material.[34] Assuming the additivity of the crystalline and amorphous contributions to the total birefringence in a semicrystalline polymer, Stein[35] proposed the following relationship for measurements above the glass transition temperature where distortion or glassy birefringence should not be present

$$\Delta_T = \phi_c \cdot f_c \cdot \Delta_c^\circ + (1 - X_c) \cdot f_{\text{am}} \cdot \Delta_{\text{am}}^\circ + \Delta_{\text{form}} \tag{10}$$

In this case, f_c and f_{am} are the crystalline and amorphous orientation functions, respectively, Δ_c° or Δ_{am}° are the intrinsic birefringence values for the perfectly oriented crystalline and amorphous phases, respectively, and ϕ_c is the crystalline volume fraction. The form birefringence is Δ_{form} and is due to the distortion of the electric field of the incident light wave at the phase boundary of geometrically anisotropic structure.[35] This latter contribution, Δ_{form}, is noted as generally being negligible for the precursor morphologies discussed here.[2] For POM, neither the value of Δ_c°

nor Δ°_{am} has been determined and will not be accomplished here, but the total birefringence will be experimentally measured for comparison purposes with the sample f_c. In extruded HDPE-stacked lamellae systems prepared by a similar process to that utilized in this report, it has been shown by Yu et al.[2] that the amorphous orientation is negligible. Although it will not be directly proven here, it will be assumed that the same holds true for these POM-stacked lamellar morphologies. This statement is in part supported by film shrinkage experiments done at temperatures of ca. 150°C, where all POM precursors essentially retained their original dimensions within ca. 2%. Thus, the birefringence is believed to be determined by the crystalline orientation, but the f_c value determined via WAXS will be relied upon in discussing the films. A Babinet compensator method was utilized to measure the film birefringence as described elsewhere.[17]

Refractometry

To determine the refractive index in all three dimensions, i.e., MD, transverse direction (TD), and normal direction (ND), a METRICON prism coupler refractometer Model 2010, equipped with a polarized laser was utilized.[36]

Small-Angle X-ray Scattering (SAXS)

SAXS was utilized to estimate the long spacing of the POM precursors. A slit collimation system of dimensions 0.03 × 5 mm was employed with a Kratky camera along with nickel-filtered Cu Kα radiation possessing a wavelength, λ, of 1.544 Å. The SAXS profiles were obtained by passing the beam along the normal direction (ND) to the film and obtaining the scan along the machine direction (MD). No desmearing of the slit-smeared intensity data was undertaken in this investigation. After correction for parasitic scatter was performed using a Lupolen standard, the scattering curves were normalized to the main beam intensity and sample thickness. The results, $I(s)$, were plotted against the angular variable,

$$s = 2\left(\sin\frac{\theta}{2}\right)/\lambda \tag{11}$$

where θ is the radial scattering angle. The long periods estimated by using the equation $\ell = 1/s^*$, where s^* is the value of s at the peak of the slit-smeared $I(s)$ vs. s plot.

Small-Angle Light Scattering (SALS)

A He-Ne laser of wavelength 6328 Å was utilized in conjunction with an openback Polaroid™ camera that directly records the H_v scattering pattern. Further details of this technique are described elsewhere.[34]

Atomic Force Microscopy (AFM)

AFM micrographs were obtained with the use of a Digital Instruments Nanoscope III Scanning Probe Microscope operated in TappingMode™. Nanosensor TESP single-beam cantilever tips possessing force constants of 35 ± 7 N/m and oscillated at frequencies of ca. 290 kHz were used. The films were placed upon glass slides using double stick tape with raster-scanning parallel to the film MD.

Differential Scanning Calorimetry (DSC)

DSC measurement was performed with a Perkin-Elmer DSC-7 operating at a cooling rate of 30°C/min utilizing sample weights of ca. 5 mg. Sample temperatures were raised to 180°C for 10 min followed by cooling to promote crystallization. The samples were then reheated to 180°C for 15 min followed by a second crystallization run. It was noted that the results of both cooling scans were analogous. All DSC scans were performed under an N_2 atmosphere. Heating scans were conducted utilizing a heating rate of 30°C/min under an N_2 atmosphere with a sample weight ca. 5 mg. The mass fraction of crystallinity using DSC was calculated from the following relation

$$X_c = \frac{\Delta H_f}{\Delta H_f^{\circ}} \tag{12}$$

where ΔH_f is the measured heat of fusion/mol from the area under the melting endotherm and ΔH_f° is the enthalpy of fusion/mol for a 100% crystalline sample. In the case of POM, the value of ΔH_f° = 9.8 kJ/mol[37] was chosen and used throughout this study. The crystallinity was determined by calculating the area under the melting endotherm for the sample using the standard supplied Perkin-Elmer software. Baseline corrections were also accomplished using this software. Instrument calibration was done with indium and tin samples at the same heating rate of 30°C/min.

RESULTS AND DISCUSSION

The molecular and thermal characteristics of the three POM resins melt extruded in this study are

Table IV Molecular Weight Characteristics for the Three POM Resins Studied

Resin	M_n (kg/mol)	M_w (kg/mol)	M_w/M_n	T_{mc} (°C)	T_m (°C)
D	78,500	125,800	1.60	134	178
E	34,700	74,400	2.14	134	178
F	19,200	130,900	6.82	137	167

displayed in Table IV. It is recognized that resin D possesses the highest M_w followed by resin F and resin E; however, resin F is shown to have the broadest MWD (ca. 5.9) of the three as discussed earlier. As pointed out, the mechanism used to produce resin F incorporates a small amount of ethylene oxide as a comonomer to add thermal stability to the chain. The consequence is that the comonomer leads to a lower melting point relative to the other two resins, as can be observed in the DSC profile given in Figure 3 for ice-water "quenched" samples of the three POM resins. However, it is noted that all three materials are characterized by sharp melting peaks where the T_m values for resins D and E are approximately at 178°C, while resin F is 166°C. Although the data is absent from this figure, but included within Table IV, the nonisothermal melt crystallization temperature (T_{mc}) is surprisingly not decreased by the additional comonomer. From our investigation, the small difference in T_{mc} should not influence the amount of time the polymer melt is allowed to relax prior to crystallization during extrusion. The reader should recognize, however, that the reported values of T_{mc} are from quiescent melts and not oriented melts such as occur upon melt extrusion. It expected that, because M_w and MWD are critical in controlling the rheological and associated relaxation behavior, it is these latter variables that will play critical roles in the resulting orientation and morphological state, as will be discussed.

As stated earlier, the planar extensional flow promotes uniaxial symmetry about the MD axis, as verified by Figure 4, which shows the WAXS pattern of a POM precursor obtained with the X-ray beam parallel to the MD. No azimuthal dependence is noted, thereby verifying MD as a symmetry axis.[1,2] This type of WAXS pattern occurred for all POM precursors extruded with this film line. In addition, refractometry was performed to determine the refractive index for all three directions (MD, TD, and ND) of a POM film. As expected for a uniaxially oriented system, the ND and TD refractive index values were equivalent (ca. 1.4741), while the refractive index along the MD was different (ca. 1.5226).

Resins D (Highest M_w, Narrow MWD)

The WAXS diffraction patterns for films D2–D5, obtained with the beam along the normal direction (ND), are shown in Figure 5(a)–(d). These resin D precursors films were melt extruded using the conditions #2–#5 described earlier in Table I. In this figure, an arrow indicates the reflection corresponding to the (100) planes. This reflection is utilized to estimate f_a and thus f_c, i.e., the

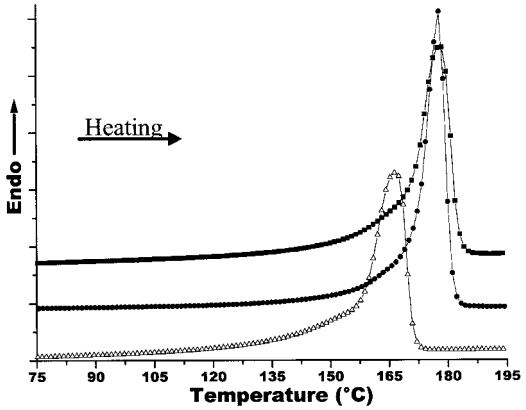

Figure 3 Second heating scans of POM (□) resin D, (●) resin E, and (△) resin F utilizing a heating rate of 30°C/min.

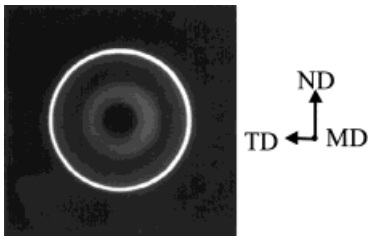

Figure 4 WAXS of an oriented POM film with X-ray beam parallel to film MD isotropic crystal orientation with respect to the ND of the film.

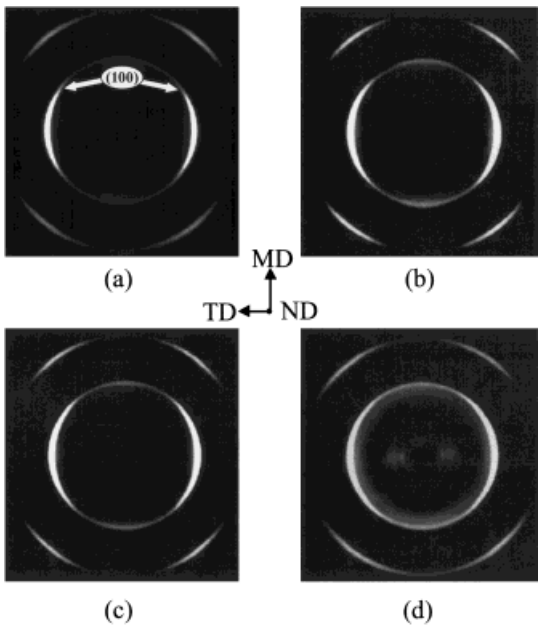

Figure 5 WAXS photographs of resin D POM films (a) D2, (b) D3, (c) D4, and (d) D5. The MD is labeled. Arrows in figure (a) indicate the reflection corresponding to the (100) set of planes.

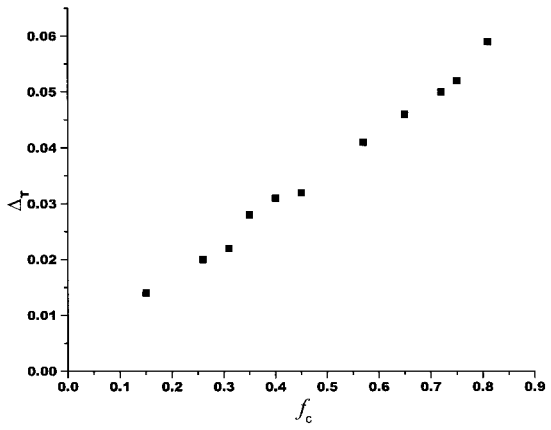

Figure 6 The measured total birefringence (Δ_T) plotted against the crystalline orientation (f_c) measured from the WAXS.

"c"-axis (chain axis) orientation with respect to the film MD. In Figure 5, the azimuthal dependence of this reflection for each of these precursors is not considerable. However, precursor D2 possesses the greatest azimuthal dependence of those shown. Recall that the azimuthal dependence can be related to f_c and thus the precursor, termed D2, produced by extrusion condition #2, is characterized by the greatest level of crystalline orientation along MD for the resin D films. The crystalline orientation for each resin D film, as measured by f_c, is listed in Table V with other pertinent film properties (Δ_T, T_m, X_c) to be addressed. These results indicate that f_c values are ranked in the following order: D2 > D1 > D3 > D6 > D4 > D5. Note that in calculating f_c for the precursors, the meridonal intensity of the (100) planes was ignored, and only the azimuthal spread of its equatorial reflection was utilized. The meridonal region of these WAXS patterns, specifically for the (100) reflection, displays different weak intensity levels between the precursors. This bimodal effect feature of "a"-axis orientation has been noted in other studies[13,14–16,44] on stacked lamellar morphologies, where the "a"-axis orientation was attributed to lamellar twisting/tilting. It is recognized in Figure 5 that the meridonal intensity is the least intense for the highest oriented sample, D2, but is most intense for the lowest oriented sample D5. This meridonal scattering intensity, indicating partial "a"-axis orientation along MD, also decreases as Δ_T increases (Table V), as would be expected. In fact, Δ_T nearly scales linearly with f_c for all the POM films studied (see Fig. 6). In contrast, neither the melting

Table V The Crystalline Orientation (f_c), Total Birefringence (Δ_T), Long Spacing (ℓ), Mass Fraction Percent Crystallinity (X_c), and Melting Point (T_m) for the Resin D Precursors

Sample	$f_{c,(100)}$	Δ_T	ℓ (A)	X_c (%)	T_m (°C)
D1	0.40	0.031	153	52	178
D2	0.45	0.032	152	52	177
D3	0.35	0.028	149	51	177
D4	0.26	0.020	154	50	179
D5	NM[a]	0.014	153	51	179
D6	0.31	0.022	152	50	178

[a] NM indicates that the azimuthal dependence was not sufficient enough to allow a reasonable estimate of f_c.

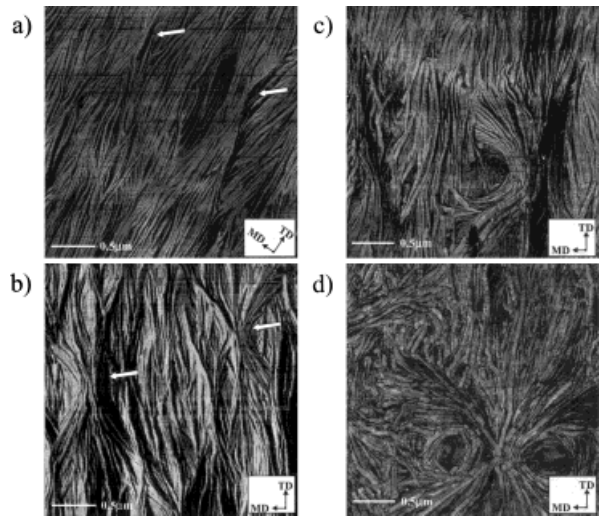

Figure 7 AFM phase images of the resin D POM films (a) D2, (b) D3, (c) D4, and (d) D5. The MD is labeled. Images are each 3 × 3 μm.

temperature (T_m), the degree of crystallinity (X_c), or the long spacing (l), change significantly as a function of the resin D processing conditions. In Table V, the measured long spacing for the resin D films remains constant at approximately 152 Å, the crystallinity is ca. 51%, and the average melting point is 178°C.

AFM micrographs of the same resin D precursors whose WAXS patterns are presented in Figure 5 are shown in Figure 7. It is apparent that a nonplanar (twisted) stacked lamellar morphology is predominant in each of these films with the average lateral (long) direction of the lamellae being oriented perpendicular to the film MD. Additionally, larger scale sheaf or fan-like morphologies, indicated by arrows, are evident in the films presented in Figure 7 where the individual fans are oriented perpendicular to the MD. Recognize that the sizes and concentration of these structures increase as either f_c or Δ_T decrease [compare the AFM micrographs in Figs. 7(a) and (d)]. In the latter case, the superstructure has the two-dimensional appearance of a spherulitic superstructure that has been described by Wunderlich.[37] In his description, it is stated that this type of spherulitic superstructure emanates (nucleates) from small crystalline lamellae or, in this particular case, more possibly from a small concentration of row nuclei. This is not the first time spherulitic[11] or sheaf-like[12] morphology has been observed in a process where crystallization of the melt occurs during the application of extrusion stress. Oriented sheaf/fan-like lamellar arrangements were reported by Hashimoto and coworkers for PB-1 blown films.[12] Spherulitic-like superstructures were also found to occur for metallocene catalyzed linear low-density polyethylene (LLDPE) blown and cast roll films where the resins possessed similarly narrow MWD values of ca. 2. In some of the LLDPE and all PB-1 films, SALS was observed to produce oriented butterfly-like patterns where the theory describing these patterns has been discussed by Hashimoto and coworkers.[12]

Figure 8(a)–(d) presents the H_v SALS patterns for the resin D films D2 through D5, respectively, the same films displayed in Figures 5 and 7. Besides the overall two-fold symmetric butterfly-type pattern, there are inner "lobes" that decrease in intensity from D2 through D5 or as f_c or Δ_T decreases. Notice that film D5 has a total absence of any inner lobe in Figure 8(d). There are also observable maxima present in the butterfly lobes of films D4 and D5; however, maxima are not present in the SALS patterns for the other two films presented in Figure 8. These two films are of a higher f_c than those that do have maxima. In an attempt to relate the proposed light-scattering theory of Hashimoto et al.[12] for oriented sheaf

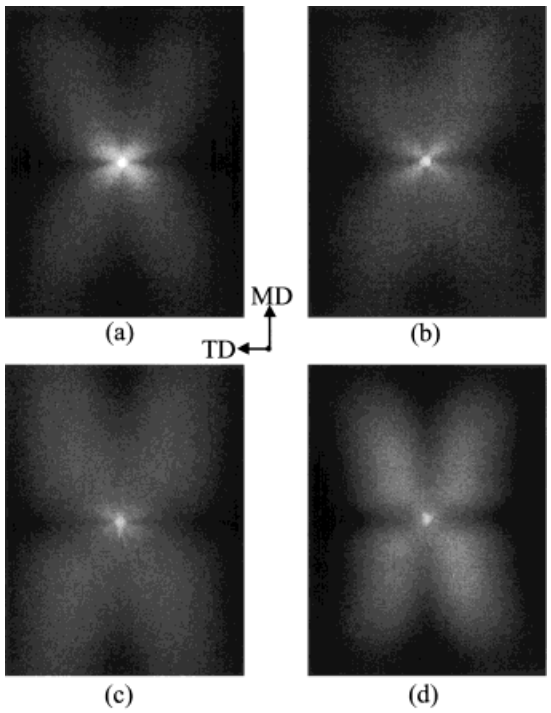

Figure 8 H_v SALS photographs of resin D POM films (a) D2, (b) D3, (c) D4, and (d) D5. The MD is labeled.

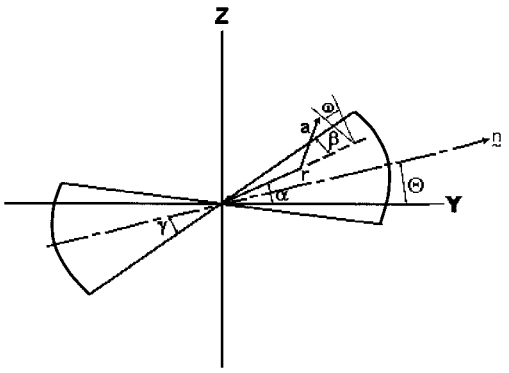

Figure 9 Oriented fan model of Hashimoto and coworkers where angle γ is half the aperture angle of the fan. The MD is along the Z-axis. Reprinted with permission from T. Hashimoto.

morphologies to our experimental H_v SALS patterns, a depiction of their oriented fan model is displayed in Figure 9, where the angle γ is half the aperture angle of the fan. This particular parameter will be the only one discussed with respect to its effects on the maxima in the H_v SALS patterns. According to this theory, as the angular spread of the oriented fan becomes smaller, γ decreases, the maxima become more elliptic and orient towards the vertical (normal to the sheaf) as well as away from the zero scattering angle ($\theta = 0$). Recalling the AFM results, the sheaf structures were observed to decrease in overall size but also to decrease in γ (angular spread) as f_c increased. Thus, based upon this theory of Hashimoto, the resin D H_v patterns should be more oriented towards the vertical (MD) as the precursor f_c increases. The particular shape of the maxima and the direction, if any, towards which the maxima orient is only evident upon examination of the patterns exhibiting maxima where the theory holds. Additionally, the overall lobes do occur at distinctly higher angles for sample D2 relative to samples D3, D4, and especially D5. This implies that sample D2 possesses smaller superstructural elements as indeed was verified earlier by AFM [recall Figs. 7(a), (c), and (d)]. In the case of the lowest oriented film, as observed via AFM and SALS, it does appear to possess the most spherulitic-like texture with distinct maxima observable in the SALS pattern. As is well established, the average radius, R, of an anisotropic spherulite can be determined from the H_v pattern[34,38] by use of the relationship

$$4.13 = \frac{4\pi R}{\lambda_m} \sin(\theta_{\max}/2) \tag{13}$$

where λ_m is the wavelength in the medium and $\theta_{\max}$ is the radial scattering angle defined by the maximum in the scattering intensity in any lobe of the fourfold symmetric H_v pattern. The value of λ_m is determined by dividing the wavelength of the incident beam (632.8 nm) by the average refractive index of the polymer, 1.55[39] (an average isotropic value). Applying this equation only to sample D5, the average spherulitic diameter for this sample is approximately 3.2 μm, which is comparable to the structure in Figure 7(d).

To better observe the decrease in superstructure size as f_c or Δ_T increases, Figure 10(a) and (b) are presented; these are AFM height images of the highest and lowest oriented resin D films (D2 and D5, respectively) using a much lower magnification scale (30 $\times$ 30 μm). Clearly, much larger superstructures occur in D5, where these are similar in size to that calculated from the SALS pat-

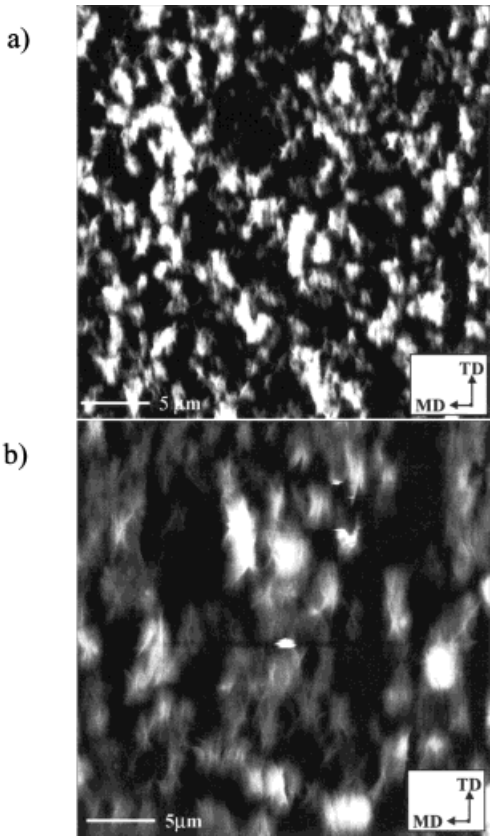

Figure 10 AFM height images of POM resin D films (a) D2 and (b) D5. The MD is labeled. Images are each 30 $\times$ 30 μm.

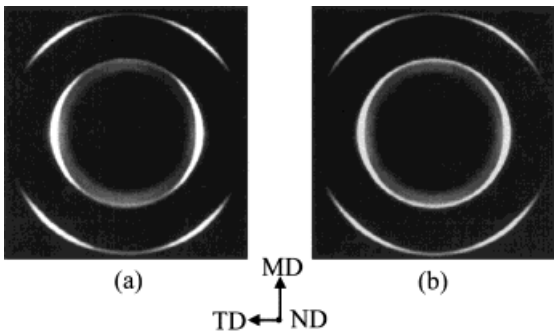

Figure 11 WAXS photographs of resin E POM films (a) E2 and (b) E4. The MD is labeled.

terns. In the higher oriented film, D2, much smaller and more numerous sheaf-like structures are evident. Thus, for these resin D films, as f_c or Δ_T increases as a result of the processing conditions, the morphology becomes smaller and less spherulitic-like moving towards a sheaf-like texture. These fans were also found to decrease in aperture angle (γ) but increase in frequency as f_c increased. Note, however, that in each case of the resin D films, the lamellar arrangement was generally stacked with the long dimension perpendicular to the MD axis even in the case of sample D5.

Resin E (Lowest M_w, Narrow MWD)

The reader will recall that the important difference between resins D and E is the value of M_w, resin E possessing a lower value than resin D. It is expected that the resin E films will possess less crystal orientation than the resin D films when processed under equal conditions. This is observed in Figure 11(a) and (b), which displays the WAXS diffraction patterns for the precursors from extrusion conditions #2, and #4, respectively, i.e., films E2 and E4. The (100) scattering reflection of the precursor E2 has slightly greater azimuthal dependence than the E4 precursor. The f_c value for precursor E2 is observed in Table VI along with other precursor characteristics for the resin E specimens. Although extrusion condition #1 was utilized for resin E to produce film E1, results shown in Table VI suggest that it possessed analogous characteristics to that of film E2. This lack of an extrusion effect between conditions #1 and #2 with respect to resin E is believed to be due to its lower M_w and relatively narrow MWD. However, as in the case of the resin D films, the birefringence values scale with the f_c values, while the long spacing, melting temperature, and crystallinity remain essentially constant between the three resin E precursors at 157 Å, 177°C, and 54%, respectively.

The morphologies of the resin E precursors are influenced by the process conditions, as can be observed in the AFM micrographs displayed in Figure 12(a) and (b). For the more oriented sample, E2, Figure 12(a) shows the structure of this sample to be a stacked lamellar morphology with evidence of twisting and tilting of the lamellae. The WAXS patterns of these samples also indicate considerable "a"-axis orientation, thus verifying there is lamellar twisting or tilting. The lower oriented film, E4 displayed in Figure 12(b), is characterized by a more isotropic lamellar superstructure similarly observed for precursor D5. In fact, a few lamellae are observed to return or tilt back along their growth direction. As already stated, such a morphology is quite atypical of flow-induced morphologies were the application of stress is known to produce higher levels of nucleation than in its absence. A similar H_v SALS pattern to the D5 film is also obtained for film E4 as shown in Figure 13(b). Note the apparent maxima in the lobes, which provide an estimated superstructure size of approximately 4.5 μm. The E2 SALS pattern, Figure 13(a), is more typical of the resin D films possessing the fan-like structures, which includes the detectable presence of the previously mentioned inner "lobes." It also displays distinct maxima in the butterfly lobes, which leads to an estimated size of roughly 2.3 μm. As expected, this value is lower than that for

Table VI The Crystalline Orientation (f_c), Total Birefringence (Δ_T), Long Spacing (ℓ), Mass Fraction Percent Crystallinity (X_c), and Melting Point (T_m) for the Resin E Precursors

Sample	$f_{c,(100)}$	Δ_T	ℓ (A)	X_c (%)	T_m (°C)
E1	0.15	0.014	157	54	176
E2	0.15	0.071	156	55	177
E4	NM[a]	0.010	157	54	177

[a] NM indicates that the azimuthal dependence was not sufficient enough to allow a reasonable estimate of f_c.

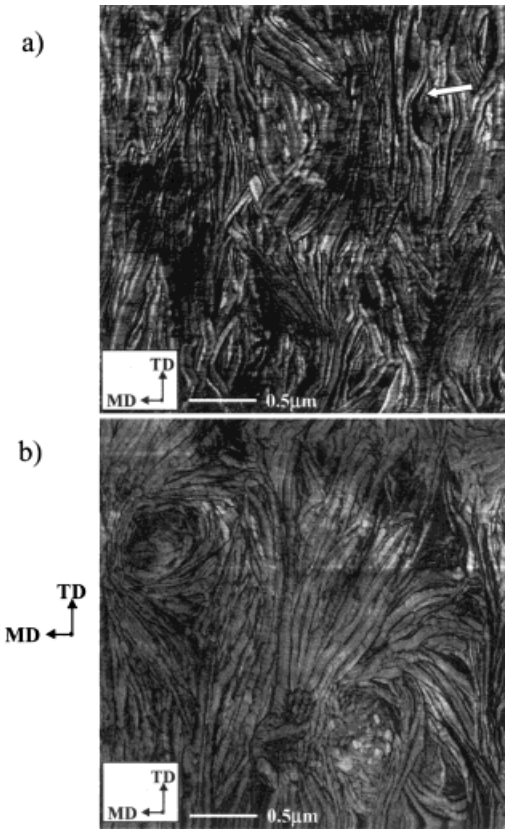

Figure 12 AFM phase images of the resin E POM films (a) E2 and (b) E4. The MD is labeled. Images are 3×3 μm.

film E4. These patterns also respond in the manner predicted by the light-scattering theory described by Hashimoto et al. regarding the lobes and their maxima moving towards the MD as the aperture angle decreases, which, in our case, is also as f_c increases. AFM height images using a larger length scale (10×10 μm) are presented in Figure 14(a) and (b) of precursors E2 and E4. In both cases, the morphologies observed here reflect those shown in Figure 12 at the higher magnification. Specifically, a sheaf-like morphology is observed in the higher oriented film while in the lower oriented film, a more spherulitic-like lamellar arrangement occurs. Additionally, the superstructure number per area or concentration appears to be greater for the film E2 vs. E4. These superstructure sizes observed via AFM correlate well with the average superstructure size calculated from the SALS photographs. It is, therefore, recognized that as f_c or Δ_T increase, the superstructure size decreases while the number of these structures increases as a result of the melt-extrusion conditions.

Resin F (Intermediate M_w, Broadest MWD)

The WAXS diffraction patterns are displayed in Figure 15 for selected resin F melt-extruded precursors that arise from the extrusion conditions F1, F2, F3, and F4 described in Table III. It is immediately evident upon examination of these figures, that each display distinctly higher azimuthal dependence of the (100) scattering reflection than has previously been observed for comparable films from either resin D or E, when processed at the same condition (#2). In fact, upon calculation of the f_c values given in Table VII along with other film properties, the results clearly reflect this statement. The resin F sample F1 possesses the highest f_c value for the films from this resin but also for any of the three resins investigated. More important, however is that, upon direct comparison of similarly extruded films, D2, E2 and F2, it is clearly evident that film F2 possesses a significantly higher f_c value than either D2 or E2. This result is an obvious consequence of the MWD difference between resin F and resins D and E. The resin F precursor f_c values are also ranked accordingly in the order F1 $>$ F2 $>$ F5 $>$ F3 $>$ F4.

The reader recalls that the presence of "a"-axis orientation was noted in both the resin D and E films from the evident meridonal intensity of the (100) reflection. Upon further examination of the resin F WAXS patterns, this type of orientation is found as well. Another similarity with the resin D films is that the intensity in the meridonal region decreases with increasing f_c, as was expected based upon the works of previous investigators.[13,17] Thus, the level of lamellar twisting, which is indicated by the presence of some "a"-axis orientation, decreases as f_c increases when

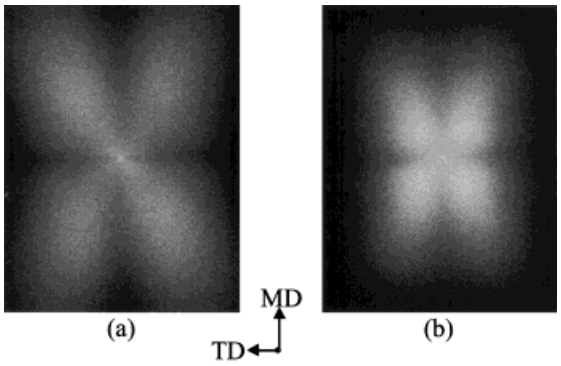

Figure 13 H_v SALS photographs of resin E POM films (a) E2 and (b) E4. The MD is labeled.

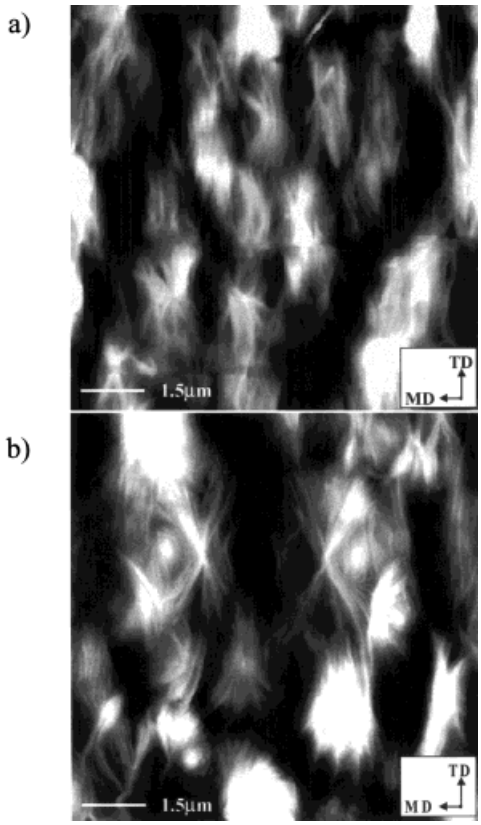

Figure 14 AFM height micrographs of POM resin E films (a) E2 and (b) E4. The MD is labeled. The images are 10 × 10 μm.

comparing resin F samples among each other. The total birefringence, as measured from the samples, also follows this trend. The long spacing, degree of crystallinity, and melting temperature do not change with extrusion conditions as observed previously, where the average values for the resin F films are 128 Å, 48%, and 166°C, respectively.

The morphologies of the same precursors presented in Figure 15 are displayed in Figure 16(a)–(e) at the higher magnification utilized previously (3 × 3 μm). A stacked lamellar morphology is present in each film where more planar lamellar textures are noted for the films F1, F2, and F5, while samples F3 and F4 have observably more twisting as shown in Figure 16(a)–(e), respectively. The precursor F1 appears to possess the most planar texture while the lamellae twist to a greater extent for the precursor F4; however, there is a detectable amount of lamellar twisting for all the resin F precursors, thus verifying the WAXS results. In contrast to the resin D and E films, an overall lack of any observable superstructure is noted in the AFM micrographs for any of the resin F films. The H_v SALS patterns also differ from those from resins D and E. Note the absence of any butterfly-type pattern for the selected resin F film results displayed in Figure 17. This is the case even for the lowest oriented precursor F4, which displays an H_v SALS pattern similar to that published by one of the authors[40] for a tubular extruded iPP precursor film. The current authors point out that the associated iPP film morphology was a stacked lamellar texture, which is of no surprise because that particular film is utilized as a precursor for iPP commercial microporous films via the MEAUS process. A similar H_v pattern occurs for sample F3, which possesses the second lowest f_c, except that the scattering is less diffuse at large scattering angles directly along the vertical or MD axis. Recognize also the trend among these H_v patterns as f_c changes. Specifically, a more rigid rod-like scattering pattern is observed for sample F1 (highest crystal orientation) although it possesses more clover-leaf like scattering with no distinct maxima.[34] These patterns become increasingly more diffuse (less clover-leaf like) as the orientation decreases and the morphology changes from planar to more twisted. However, the light-scattering theory accounting for this behavior has not been developed, and will not be undertaken here.

AFM height images at lower magnifications for these resin F precursors are displayed in Figure

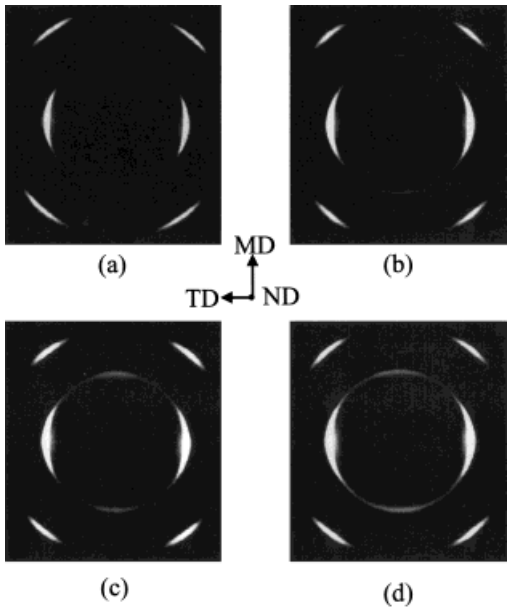

Figure 15 WAXS photographs of resin F POM films (a) F1, (b) F2, (c) F3, and (d) F4. The machine direction is labeled MD.

Table VII The Crystalline Orientation (f_c), Total Birefringence (Δ_T), Long Spacing (ℓ), Mass Fraction Percent Crystallinity (X_c), and Melting Point (T_m) for the Resin F Precursors

Sample	$F_{c,(100)}$	Δ_T	ℓ (A)	X_c (%)	T_m (°C)
F1	0.81	0.059	128	48	165
F2	0.75	0.052	129	48	165
F3	0.65	0.046	128	47	166
F4	0.57	0.041	126	48	167
F5	0.72	0.050	127	47	165

18(a) and (b). In the case of film F1, a highly oriented fibril texture appears to be present. This morphology is somewhat apparent in the previous higher magnification phase image of this film, Figure 16(a). Recalling this figure, the reader will recognize that there is the appearance of a larger

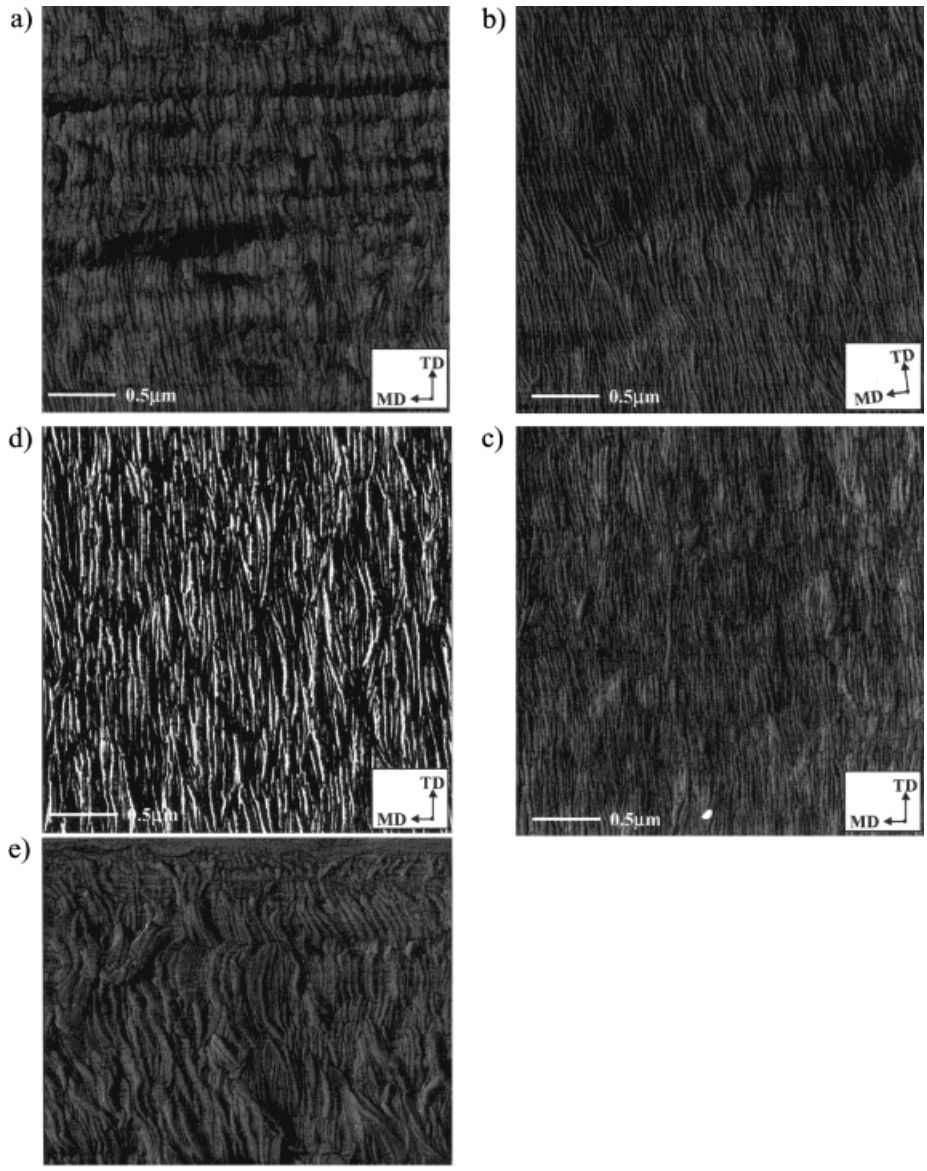

Figure 16 AFM phase images of the resin F films in order of decreasing f_c values (a) F1, (b) F2, (c) F5, (d) F3, and (e) F4. The MD is labeled. Images are 3 × 3 μm.

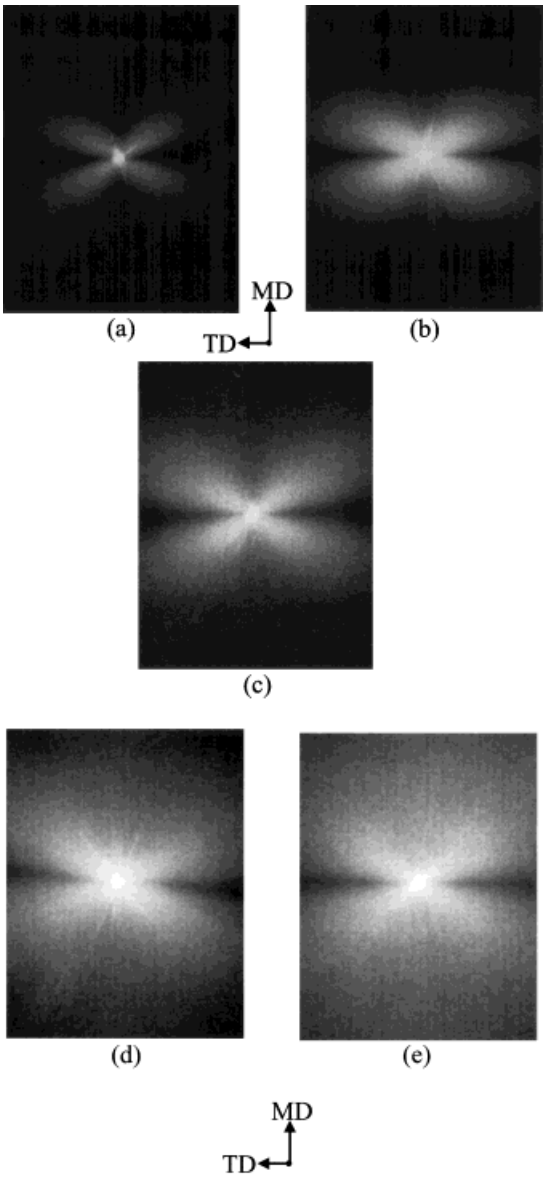

Figure 17 H_v SALS photographs of resin F POM films arranged according to decreasing f_c or Δ_T (a) F1, (b) F2, (c) F5, (d) F3, and (e) F4. The MD is labeled.

scale layer-like morphology with its long axis aligned parallel with the MD, which is better observed via the height image in Figure 18(a). The other film, F3, appears to have no trace of such structures. Upon reexamination of the higher resolution AFM micrograph in Figure 18(b), there is a lack of any observable layer-like structure. However, in all AFM micrographs there is an absence of any visible "shish" or row nuclei, and the WAXS patterns do not display additional sharp equatorial reflections superimposed upon the (100) reflection. Sharp equatorial superimposed reflections in WAXS patterns have been shown to occur in the case of HDPE tubular films that did possess visibly evident shish-kebob morphologies.[2] Thus, the observed morphologies may not contain long fibril structures based on the above WAXS and lack of any observable row nuclei in the AFM micrographs. However, if there are large long fibrillar nuclei in film F1, they would be detrimental to the formation of a microporous morphology upon uniaxial-stretching. This is due to the "pinning" effect caused by these structures during stretching thus hindering lamellar separation.[41] This will be addressed in the second report of this study,[9] where a selected number of the resin D and especially resin F precursors will be followed for the effects of annealing and stretching variable combinations on the resulting morphology and microporosity.

As pointed out, the differences in the resin characteristics influence the film morphology and orientation state of the precursors as well as the long spacing, melting temperature, and crystallinity. The long spacing, melting temperature,

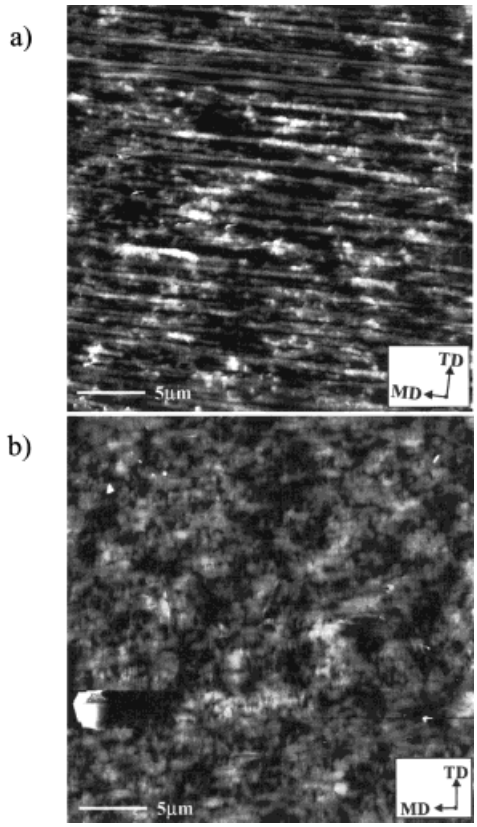

Figure 18 AFM height images of the resin F POM films (a) F1 and (b) F2. The MD is labeled. Images are each 30 × 30 μm.

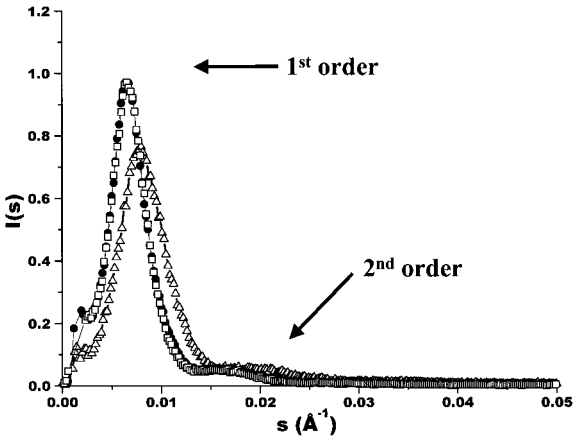

Figure 19 The slit-smeared SAXS spectra from the highest oriented POM films (□) D2, (●) E2, and (△) F2.

and crystallinity are, of course, a consequence of the added comonomer present in resin F resulting in a disruption of the chain symmetry thereby leading to greater imperfection in the crystalline phase. This greater imperfection in the crystalline phase then produces a lower melting temperature and level of crystallinity vs. precursors from the resins polymerized without the presence of the comonomer (resins D and E). Because the defects caused by the added comonomer are likely to be excluded from the crystalline phase, the crystalline lamellae will be smaller as reflected by the smaller long spacing, recall Tables V–VII. This result is also shown in Figure 19, where the corresponding SAXS profile of sample F2 is given for the slit-smeared intensity vs. scattering vector, s. The corresponding SAXS profiles for the similarly extruded samples D2 and E2 are also displayed for comparison purposes. These SAXS profiles were obtained by passing the X-ray beam along the ND and obtaining the scan along the MD. As might be expected, these profiles clearly show a well-defined first-order peak along with a weaker second-order peak. [Note that this data is slit-smeared, and thus the first- and second-order peaks are not as prominent (intense) or narrow as they would be if desmearing had been undertaken.] The SAXS data in addition to that presented in Tables V–VII indicates the effect the ethylene oxide comonomer present in resin F has on the lamellar thickness. Neglecting differences in the long spacing, both resin D, E, and F precursors have similar SAXS profiles suggesting that the resins, when extruded under analogous conditions, possess similar lamellar morphologies.

When comparing similarly extruded films from resins D and E, the resin parameter that did affect the structural features and orientation state of the precursors was the value of M_w (recall that both resins possessed an MWD of ca. 2). The value of M_w has been found to influence film properties for a number of semicrystalline polymers.[1,2,13–15,17] This outcome is principally due to the melt-relaxation time differences M_w as is recognized in Figure 20 where the complex viscosity data is displayed as a function of frequency for resins D, E, and F. The viscosity curves were fitted with the three-parameter CY equation, eq. (1), and the recoverable shear strain parameter (RSP), eq. (4), in the low frequency range (0.05 radian/s). The resulting fitting curves for the CY equation are shown as continuous lines in Figure 20 while the zero shear viscosity (η_o), characteristic melt-relaxation time (τ_n), fitting parameter "a," and the recoverable shear stain parameter (RSP) values are also included in the table inserted within Figure 20. Of particular interest are the CY relaxation time parameter (τ_n) and RSP values for the specific resins. In the case of the CY τ_n values, the higher M_w narrow distribution resin D is, as expected, greater than the lowest M_w narrow distribution resin E by a factor of roughly 5. Additionally, the RSP value, a measure of the melt elasticity and recovery or relaxation time, is approximately two times greater for resin D than resin E. The CY τ_n values and RSP data comparisons provide strong support for a much lower elastic character for resin E, as would be

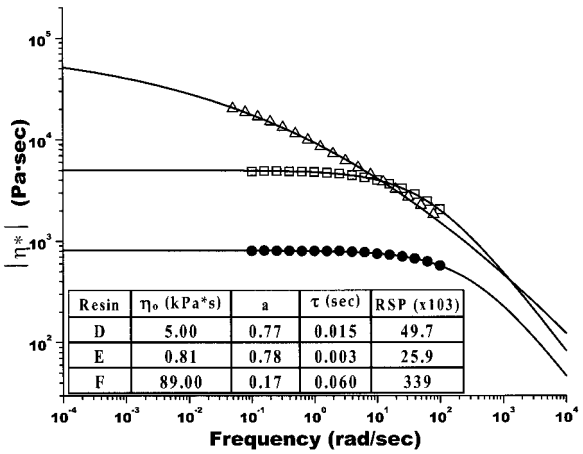

Figure 20 Complex viscosity vs. frequency data for resins (□) D, (●) E, and (△) F from this study obtained via dynamic oscillatory shear measurements at 180°C. A table of the CY parameters and the RSP value are also included.

expected based on the lower M_w of this resin in contrast to the higher molecular weight resins. This suggests why given a specific extrusion condition, the resin E precursor, is less oriented than the resin D sample. Thus, resin E has the ability to undergo relaxation more quickly and thereby develop a more "quiescent-like" texture following nucleation and growth of the crystalline phase.

The CY τ_n values are also different for resins D and F; in the case of the latter resin, it is approximately four times greater than that for resin D. The fact that the calculated value of η_0 is higher for resin F than resin D is a bit perplexing since this parameter typically scales with M_w to the 3.4 power. The difference, however, may possibly be due to a small amount of long chain branching in resin F which, if present, could certainly promote a higher value of η_0 than for resin D. The RSP value provides further validation to these melt-flow behavior differences, with resin F possessing a value approximately 13 times greater than the lowest M_w resin E, and 6.8 times that of resin D! This higher melt elasticity explains why, given a specific extrusion condition, the resin F precursor F2 possesses a higher f_c, Δ_T, and more planar lamellar texture than either films D2 or E2. As previously suggested, this directly reflects the influence a broader MWD has on the melt-flow behavior, and thus the morphological features and orientation state upon crystallization under stress. Therefore, for these resins, either the RSP value or the CY parameter τ_n provides accurate means to evaluate the melt-relaxation response of a polymer. In the case of the CY fit utilized here, recall that the parameter "n" was set equal to 2/11. This value appears to provide accurate CY fits for the POM resins studied here. Interestingly, the CY parameter "a" also provides information regarding resin characteristics because it is inversely related to the MWD breadth; thus, the broader the MWD, the lower the value of "a."[42] This is reflected in the table presented within Figure 20. It is noted that while this parameter is roughly equivalent for the resins D and E, which do possess essentially identical MWD, the parameter is, as expected, lower for resin F by a factor of 4.6 due to this resin's broader MWD. The CY "a" parameter values for these commercial POM resins are somewhat consistent with those reported for PE resins of similar MWD.[43] Specifically, metallocene catalyzed PE resin, known for MWD ca. 2, generally possess values of $0.5 < a < 0.7$, which are quite consistent with resin D and E in both MWD and the parameter "a." For broader PE resins, such as those prepared via the Ziegler-Natta catalysis, these are characterized by "a" values ranging from 0.35 to 0.5. Furthermore, the CY "a" parameter for chromium oxide PE resins, known as even broader MWD resins, often range from 0.12 to 0.25. Thus, even if the POM resin characteristics were unknown, a qualitative understanding of the melt-flow behavior (τ_n) and MWD could be easily obtained for this linear system.

As in prior investigations,[1,2,13,44] it has been shown in this study that the applied stress field, as a function of the process conditions, is important in determining the structure/orientation of the extruded films. The melt-relaxation behavior is also relevant to the structural development of the crystallized material. Thus, how much orientation can be maintained in the final product is strongly dependent upon how fast and how early the oriented melt is quenched and crystallized. With this consideration, a larger quench height would allow greater time for the polymer melt to relax and thus crystallize slower with less orientation. In contrast, a faster line speed would shorten the time scale for the melt to reach the cooling ring. Additionally, a faster line speed increases the line stress applied to the melt, producing greater orientation within the polymer melt as it exits the die. Also, the viscosity of the melt as it exits the die will affect the line stress, and, because viscosity is a function of temperature, a lower melt temperature at the die exit will result in a higher line stress and, therefore, promote a higher oriented melt during crystallization. From the analysis of the f_c values, in Tables V–VII, for the four extrusion variables discussed, it was noted that line speed in conjunction with extrusion rate have a much greater influence than quench height and melt temperature for the extrusion window investigated. However, it is clearly evident the influence of M_w and MWD influence on the melt-relaxation time are more critical to the end film orientation and morphological features. In fact, as a result of the broader MWD of resin F compared with the other POM resins, planar stacked-lamellar morphologies characterized by relatively high f_c values were obtained in all but sample F4.

CONCLUSIONS

From the selected POM resins and their characteristics, this study provided a degree an under-

standing regarding the influence the M_w and MWD have on the resulting film solid-state structure. Specifically, a number of different types of morphological features were found for the three POM resins processed by tubular extrusion. In fact, it could be concluded that almost a continuous spectrum of morphologies were obtained, which spanned the spherulitic-like textures to the planar stacked-lamellar morphology with the possible production of fibrillar morphology. This latter case is suggested not to be present for the F1 precursor based upon the results utilizing the techniques of AFM at higher magnifications and WAXS. This so-called spectrum of morphologies was found to be dependent upon both the molecular characteristics of the resin, as well as the melt-extrusion conditions, which control the line-stress applied to the melt during crystallization. In the case of the latter, the processing conditions were found to influence the precursor properties where a higher melt temperature, slower line speed/extrusion speed, or higher quench height produced a lower f_c or Δ_T value and more quiescent-like (spherulitic) morphology. These observations clearly support the effect of extrusion stress on the structure including lamellar twisting for this polymer.

The resin characteristic M_w was found to be responsible for the differences in morphological features and the orientation state between similarly processed precursors of resin D and E (recall the MWD values of either resin were ca. 2). Resin D possessed the higher M_w of the two resins, and thus those films had less of a quiescent-like morphology with higher f_c and Δ_T values. The higher MWD of resin F was noted to produce a more planar-like lamellar morphology with higher f_c and Δ_T values than resin D which possessed nearly the same value of M_w. The effects of the molecular characteristics on the morphology and orientation state of the melt-extruded precursor were found to be a consequence of their influence on the melt-elasticity or relaxation time. The slower the relaxation time or the more elastic the melt, the higher its orientation at the time of crystallization, thereby resulting in a more planar lamellar structure and higher f_c and Δ_T. The morphological features and orientation state have been observed to influence the properties of microporous films made from PMP[1] and HDPE[2] extruded precursor films by further annealing and uniaxial stretching; thus, it is believed that the same properties will affect the ability to form microporous membranes from these POM films to be addressed in the subsequent article.

The authors would like to thank the Celgard Corporation LLC for their continuing financial assistance for this project as well as the informative discussions that have taken place with them. Dr. Kurt Jordens is thanked for his many helpful discussions and suggestions. The authors also thank Stephen McCartney for aiding in attempts at TEM analysis, as well as instruction in the use of AFM.

REFERENCES

1. Johnson, M. B.; Wilkes, G. L. J Appl Polym Sci, in press.
2. Yu, T. H.; Wilkes, G. L. Polymer 1996, 37, 4675; Erattum 1997, 38, 1503; J Rheol 1996, 40, 1079.
3. Boyd, R. H. Polymer 1985, 26, 323; Polymer 1985, 26, 1123.
4. McCrum, N. G.; Read, B. E.; Williams, G. Anelastic and Dielectric Effects in Polymeric Solids; Wiley: New York, 1967.
5. Celgard Corporation LLC, Company product literature.
6. Garber, C. A.; Clark, E. S. J Macromol Sci-Phys 1970, B4, 499; Int J Polym Mater 1971, 1, 31.
7. Quynn, R. G.; Brody, H. J Macromol Sci-Phys 1971, B5, 721.
8. Strathmann, H. Synthetic Membranes: Science, Engineering and Applications; Bungay, P. M.; Lonsdale, H. K.; de Pinho, M. N., Eds.; D. Riedel Publishing Co.; 1983.
9. Johnson, M. B.; Wilkes, G. L.; J Appl Polym Sci, submitted.
10. Stehling, F.; Speed, C.; Westerman, L. Macromolecules 1981, 14, 698.
11. Johnson, M. B.; Wilkes, G. L.; Sukhadia, A. M.; Rohlfing, D. C. J Appl Polym Sci 2000, 77, 2845.
12. Hashimoto, T.; Todo, A.; Murakami, Y. J Polym Sci Polym Phys Ed 1977, 15, 501.
13. Keller, A.; Machin, M. J Macromol Sci Phys 1967, B1, 153.
14. Aggarwal, S. L.; Tilley, G. P.; Sweeting, O. J. J Appl Polym Sci 1959, 1, 91.
15. Keller, A.; Kolnaar, H. Materials Science and Technology A Comprehensive Treatment; John Wiley and Sons: New York, 1997, p. 189, vol. 18.
16. Pazur, R.; Prud'homme, R. Macromolecules 1996, 29, 119.
17. Wilkes, G. L. Encyclopedia Polymer Science and Engineering, John Wiley & Sons, Inc.: New York, 1988, p. 542, vol. 14.
18. Maddams, W. F.; Preedy, J. E. J Appl Polym Sci 1978, 22, 2721.
19. Odian, G. Principles of Polymerization; John Wiley & Sons: New York, 1991, 3rd ed.

20. Graessley, W. W. Adv Polym Sci 1974, 16, 1.
21. Graessley, W. W. J Chem Phys 1967, 47, 1942.
22. Hieber, C. A.; Chiang, H. H. Rheol Acta 1989, 28, 321.
23. Hieber, C. A.; Chiang, H. H. Polym Eng Sci 1992, 32, 931.
24. Cox, W. P.; Merz, E. H. J Polym Sci 1958, 28, 619.
25. Macosko, C. W. Rheology: Principles, Measurements, and Applications; Wiley-VCH Publishers: New York, 1994.
26. Uchida, T.; Tadokoro, H. J Polym Sci Part A-2 1967, 5, 63.
27. Jungnitz, S.; Jakeways, R.; Ward, I. M. Polymer 1986, 27, 1651.
28. Enns, J. B.; Simha, R. J Macromol Sci-Phys 1977, B13, 25.
29. Zihlif, A. M. Mater Chem Phys 1985, 13, 21.
30. Nakagawa, K.; Yamamoto, F.; Takeuchi, Y.; Yamakawa, S. J Polym Sci Polym Phys Ed 1985, 23, 1193.
31. Stein, R. S.; Norris, F. H. J Polym Sci 1956, 21, 381.
32. Stein, R. S. J Polym Sci 1958, 31, 327.
33. Stein, R. S. J Polym Sci 1958, 31, 335.
34. Wilkes, G. L.; Stein, R. S. Structure and Properties of Oriented Polymers; Ward, I. M., Ed.; Applied Sci Pub: London, 1997, 2nd ed.
35. Stein, R. S. Newer Methods in Polymer Characterization; Wiley-Interscience: New York, 1964, chapt 4.
36. For more information, see http://www.metricon.com.
37. Wunderlich, B. Macromolecular Physics; Academic Press: New York, 1973, 1976, 1986, vols. 1, 2, 3.
38. Samuels, R. J. Structured Polymer Properties; Wiley Interscience: New York, 1974, p. 82.
39. Brandrup, J.; Immergut, E. H., Ed.; Polymer Handbook; Wiley-Interscience: New York, 1975, 2nd ed.
40. Manzione, L.; Jameel, H.; Wilkes, G. L. J Polym Sci Polym Lett 1978, 16, 237.
41. Yu, T. H. Ph.D. Dissertation (advisor: G. L. Wilkes) Virginia Tech, 1995.
42. Janzen, J.; Rohlfing, D. C. J Rheol, submitted.
43. Rohlfing, D. C.; Janzen, J. Metallocene Based Polyolefins—Preparation, Properties and Technology; Scheirs, J.; Kaminsky, W., Eds.; John Wiley and Sons, Ltd.; Chichester, 1999, p. 419, vol. 2.
44. Choi, K.; Spruiell, J. E.; White, J. L. J Polym Sci Polym Phys Ed 1980, 20, 27.